JOURNAL OF PROPULSION AND POWER
Vol. 18, No. 3, May–June 2002

Elliptic Coflow Effects on a Circular Gas Jet Flame

Ahsan R. Choudhuri,* Sayela P. Luna,† and S. R. Gollahalli‡
University of Oklahoma, Norman, Oklahoma 73019

The effects of elliptic coflow on the structure of a propane jet flame are presented. The interaction of a fuel jet and a coflow in the shear layer enhances the mixing behavior of the flowfield and affects the combustion characteristics of diffusion flames. Nonaxisymmetric exit jet geometries are characterized by better mixing and increased fluid entrainment into the jet core, which is desirable for low pollution from a diffusion-controlled combustion environment. In the present study the interaction of an elliptic coflow with a propane jet flame issued from a circular tube burner has been studied. Pollutant emission, flame radiation, flame structure, and soot concentration have been measured. The fuel jet exit Reynolds number is 2.7×10^3, and the exit Reynolds number for the coflow is 4.01×10^3 and 8.02×10^3 based on the minor and major axis, respectively. The results are compared with the measurements from the experiments on the same burner in a circular coflow. The pollution characteristics and the flame structure of the flame in the elliptic coflow are significantly different from those in the circular coflow. The nitric-oxide emission is higher, and the carbon-monoxide emission is lower in the elliptic coflow than in the circular coflow. The elliptic coflow flame produces less soot than the circular coflow flame.

Nomenclature

d_{cfc}	=	circular coflow diameter
d_j	=	burner diameter
F	=	radiative heat loss fraction
Re	=	Reynolds number
Re_j	=	jet exit Reynolds number
r	=	radial distance
U_c	=	coflow velocity
U_j	=	fuel jet velocity
w	=	soot concentration

Introduction

MANY practical combustor systems employ a diffusion-controlled flame configuration for energy release. In this configuration generally the fuel is injected as a jet, and the surrounding air is entrained into the fuel core through turbulent mixing and molecular mixing. Hence, the combustion process is fluid dynamically controlled, and instead of chemical kinetics mixing rate of fuel and air limits the rate of combustion. The emissions of combustion pollutants such as CO and NO_x from these combustion systems largely depend on the reactant mixing characteristics. The CO and NO_x emissions from combustion systems can be reduced if fuel-air mixing rates at different zones of the flame are controlled rationally. This generally requires a more complicated combustion system design such as staged combustion. On the other hand, postcombustion removal of pollutants is possible through catalytic conversion or exhaust gas-processing techniques. These, however, require a high setup and maintenance cost. A cost-effective way is to modify the burner geometry to enhance mixing through an alteration of the near-burner flowfield characteristics. One such approach is to use nonaxisymmetric geometries. Several previous investigations conducted in the Combustion and Flame Dynamics Laboratory of the University of Oklahoma have shown promising improvements of combustion systems through the use of nonaxisymmetric burner configurations.[1–4] The manipulation of coflow to improve the combustion characteristics of diffusion flames is also a potential technique. The use of nonaxisymmetric coflow could enhance mixing rates of fuel and air because of the higher air entrainment rate through an augmented interaction of shear layers. Numerous studies are available in the literature regarding the characteristics of the diffusion flames with coflow: however, none of them has employed nonaxisymmetric geometries for the annular coflow. Because a nonaxisymmetric jet inherently produces a higher entrainment than a circular jet, we can expect that a nonaxisymmetric coflow will yield better mixing of fuel and air; however, this concept is yet to be tested.

Several nonaxisymmetric geometries are usually considered, which include elliptic, rectangular, and triangular shapes with a small aspect ratio of 2–5. Some researchers[5] have stated that the elliptic jet entrainment rate is about three to eight times that of the circular jet of the same equivalent diameter. Schadow et al.[6] have found that elliptic jet combustion efficiency is 10% higher than that of circular jets as a result of better mixing. Motivated by this issue, this study was aimed to understand the effects of a nonaxisymmetric coflow on flame characteristics of hydrocarbon diffusion flames. The primary objective of this research is to investigate the effects of nonaxisymmetric (elliptic) coannular flow on circular jet flame characteristics, which include flame length, flame stability, radiation emission, spectral radiation characteristics, pollutant emission indices, and in-flame temperature and concentration profiles.

Background

Coaxial jets, in which annular jets surround a central round jet, arise in many practical combustion applications. For example, in utility boilers, a typical flow configuration consists of a central fuel jet surrounded by one or several annular flows. The large-scale, nearly axisymmetric vortex rings that exist in circular coannular flows produce instantaneous regions of high fuel concentration. The complex fuel-vortex interactions cause fuel particles to be flung outward on the downstream side of each vortex ring.[7–9] Because

Presented as Paper 2001-0977 at the AIAA 39th Aerospace Sciences Meeting and Exhibits, Reno, NV, 12–15 January 2001; received 18 June 2001; revision received 9 November 2001; accepted for publication 12 November 2001.

*Research Assistant, Combustion and Flame Dynamics Laboratory, School of Aerospace and Mechanical Engineering; currently Assistant Professor, University of Texas at El Paso, El Paso, Texas 79968-0521. Member AIAA.

†Research Assistant, Combustion and Flame Dynamics Laboratory, School of Aerospace and Mechanical Engineering; currently Engineer II, Schlumberger, Inc., 14910 Airline Road, Rosharon, TX 77583.

‡Lesch Centennial Chair Professor, Combustion and Flame Dynamics Laboratory, School of Aerospace and Mechanical Engineering. Associate Fellow AIAA.

the pollutant formation process in combustion strongly depends on the local stoichiometry, it is desirable to control the fuel-air mixing to effectively reduce pollutant emission.

Passive control of fuel-air mixing using a nonaxisymmetric jet-exit geometry is an attractive pollution abatement technique. For instance, the injection of longitudinal and azimuthal vortices in the jet shear layers from an elliptic coflow can control the mixing of fuel and air, because these vortices are formed in the elliptic jet as a result of asymmetric self-induction of the vortex ring structures.[5,10] The jets issued from nonaxisymmetric exits are three-dimensional because of the asymmetry in the radial and azimuthal directions. A nonaxisymmetric jet has three distinct regions[11,12]: potential core, a region where the axial velocity is equal to the exit axial velocity; characteristic decay region, where the axial velocity depends on the geometry of the jet exit, the shear between the jet and surroundings lead to a phenomenon known as axis-switching, and large-scale structures are dominant; axisymmetric decay region, where the flow approaches axisymmetry and the velocity profiles in both the major and minor axis planes are similar and vortex structures decay into fine-scale turbulence.

The asymmetry causes instability in the flowfield at the jet exit, and hence a nonaxisymmetric jet tends to remove its instability by becoming symmetric downstream. This occurs as the major axis becomes small and the minor axis becomes large in order to become symmetric leading to axis-switching. Ho and Gutmark,[5] Hussain and Hussain,[10] Sforza et al.,[11] Quinn,[12] and Gollahalli et al.[13] have shown that an elliptic jet has a faster growth on its minor axis than on its major axis. Hussain and Hussain[10] have noticed that the axis-switching continues up to 100 equivalent exit diameter of the elliptic nozzle in their study on air and water jets. Krothapalli et al.[14] have reported that the axial location of the crossover point is directly proportional to the initial aspect ratio of the elliptic nozzle. Ho and Gutmark[5] have reported that at the low-frequency range the crossover point occurs at the end of the potential core and in the higher-frequency range the crossover point occurs at the middle of the potential core.

The different growth rates on the major and minor axis, axis-switching, and instability of a nonaxisymmetric jet lead to a high entrainment of the surrounding air. As the major and minor axes switch roles, vortices are shed, and these act as a pumping device to mix the jet and ambient fluids. As the major axis shrinks, surrounding air is brought toward the jet centerline, and at the same time the jet fluid is carried outward by the expansion on the minor axis.

Schadow et al.[6] have found that elliptic jets burn 10% more efficiently than circular jets as a consequence of better mixing of fuel and air. Prabhu and Gollahalli[15] have found that the flames from elliptic nozzles yield a higher temperature and are less stable than circular flames. Gollahalli et al.[13] showed that a 3:1 aspect ratio elliptic jet flame has a lower flame stability, produces higher temperature, yields less soot concentration, and radiates less than a circular jet of equivalent exit area. Kamal[16] has also found that, in general, small noncircular nozzles entrain more secondary air, produce a higher peak flame temperature, and emit more CO_2 and less NO than a circular jet flame. In addition, he has also reported that as the Reynolds number increases the benefits of ellipticity decrease. Therefore, it is necessary to keep the jet-exit Reynolds number below an optimum value to take full advantage of the burner shape.

Experimental Setup

The burner assembly with a coflow duct was located in a vertical steel combustion chamber (Fig. 1a) of 76 × 76 cm cross section and 163 cm height and was protruded 14.5 cm above the chamber floor. The coflow duct with an elliptic exit was made by rolling an aluminum sheet over wooden mandrels having a computer generated elliptic cross section. Circular coflow ducts were produced similarly. Figure 1b shows the elliptic and circular coflow ducts. Both the circular and elliptic coflow ducts had the same exit area. The chamber was fitted with rectangular windows of dimensions 20 × 20 × 145 cm on all of its four sidewalls. Three of the windows were fitted with Pyrex plate glass, and the fourth was fitted with a slotted metal sheet for introducing probes. Air was induced by natural convection into the test chamber through a 20-cm-diam circular opening in the base plate. Three layers of fine-wire-mesh screens were used to provide a uniform flow as indicated by the velocity profile across the test chamber measured with a hot-wire anemometer while a flame at $Re = 3 \times 10^3$ was burning inside the chamber. The top of the combustion chamber was connected to the atmosphere through an exhaust duct. A relay-operated butterfly valve was used to open the exhaust duct during experiments. The fuel used in this experiment was propane (95% C_3H_8, 3% CH_4, 1% C_2H_6, 1% C_4H_{10}). Hydrogen (98%+) was used to anchor the flame in order to avoid lift off, because at a high coflow jet velocity (3.44 m/s) the flame tends to lift off and eventually blow out. [The initial experiments showed that the effects of coflow on flame characteristics were dominant at high coflow Reynolds numbers ($>2.5 \times 10^3$). To access this coflow Reynolds-number regime, the flame had to be stabilized using hydrogen. Because this investigation presents a relative study, it is expected that the effects of hydrogen on the local flame characteristics remain same in all three configurations.] The energy contribution of hydrogen was less than 2.5% of the total energy input to the burner.

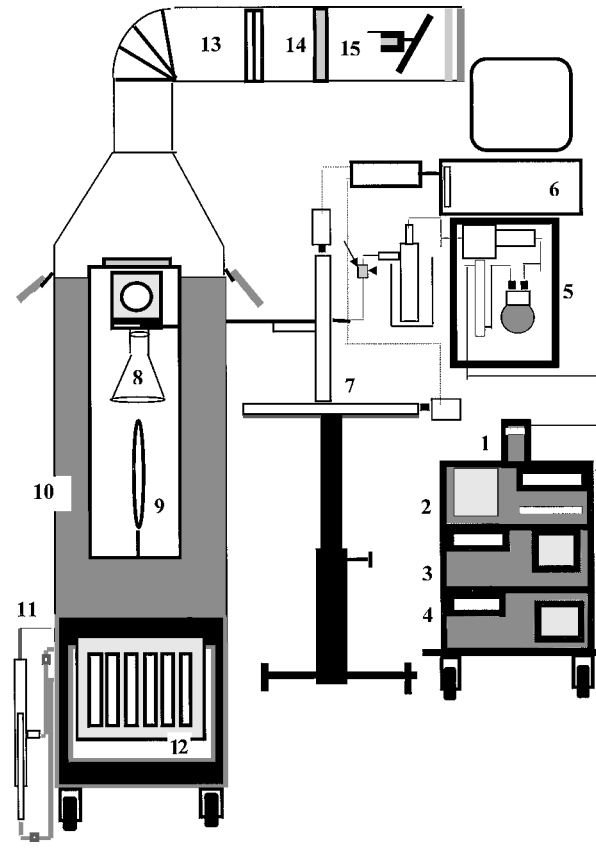

1. Oxygen Analyzer 2.NO-NO_x Analyzer 3. CO_2 Analyzer 4. CO Analyzer
5. Exhaust Treatment System: Particulate Filter, Ice-Bath, Vacum Pump
6. Data Acquisition System 7. Stepper Motor Driven 2-D Traverse
8. Exhaust Collection Cone 9. Flame with Burner 10. Combustion Chamber
11. Mixing Device 12. Rotameters 13. Damper 14. Filter 15. Relay Valve

Fig. 1a Experimental setup.

For measuring exhaust emissions a quartz flue gas collector was mounted over the visible flame and axially aligned with the burner. A sample profile across the collector exit diameter showed a variation of less than 1.5% in species concentrations, and hence the center point data were treated as the average representative values. Gas samples were collected from combustion products through an uncooled quartz probe of tip diameter 1 mm and treated to remove particulate and moisture with a series of filters and an ice-chilled moisture trap. The sampling flow rate was adjusted such that the suction and the local freestream velocities in the flowfield were close enough to ensure isokinetic sampling.[17] A chemiluminescence analyzer was used to measure the concentration of NO and NO_x. Two

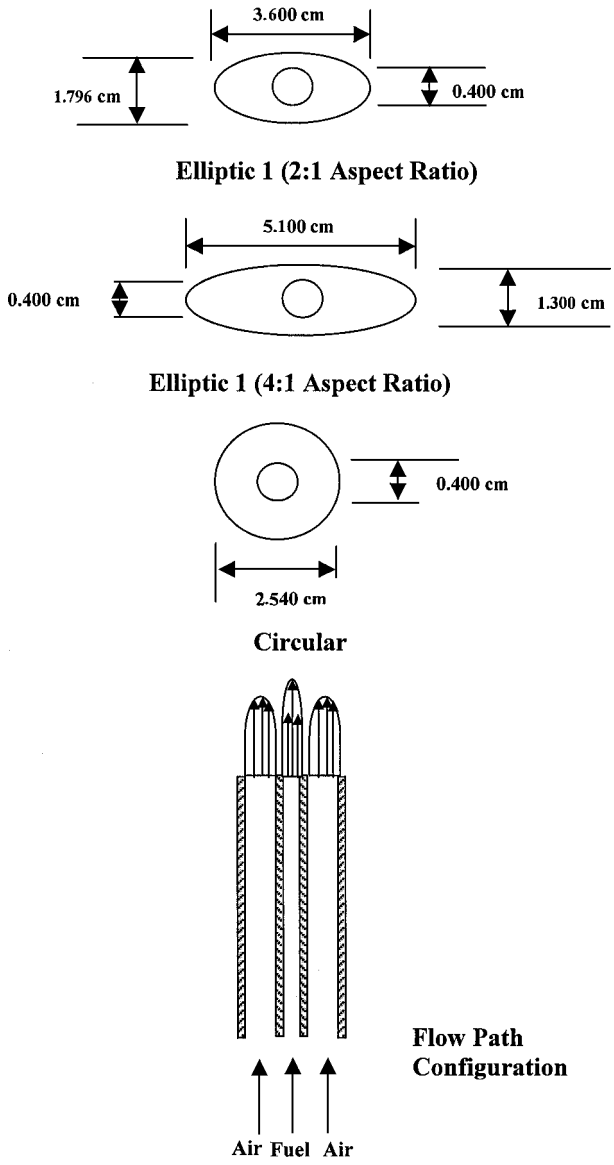

Fig. 1b Details of elliptic and circular coflow ducts.

nondispersive infrared analyzers were used to measure the concentration of CO and CO_2. For measuring species concentrations inside the flames, another uncooled quartz probe was used. The inside diameter of this sampling probe was increased from 0.5 mm at the probe inlet to 6 mm over a short distance of 20 mm, which allowed a sudden expansion of the gas sample, thus freezing its composition. The probe was mounted on a computer-controlled, stepper-motor-driven two-dimensional traversing mechanism, which had a positional accuracy of 0.13 mm/m. The sample was analyzed using the same analyzers used in the exhaust emission measurements. Neglecting the gradient broadening effect, the uncertainties in the species concentration measurements were estimated to be less than 9% of the mean value. To measure the thermal structure of the flame, a silica-coated platinum-platinum 13% rhodium (Type R) in-house-made L-shaped thermocouple probe with a wire diameter 127 μm and a bead diameter 280 μm was used. The thermocouple was mounted on the same two-dimensional traverse used for the species concentration measurements. The output was sampled at 1 kHz, on-line averaged over one second, and corrected for radiation and conduction losses. Data were acquired over a period of 20 s at each measurement location, processed, and averaged off-line. For measuring flame radiation a wide-angle (150 deg) highly sensitive pyrheliometer of absorptivity 0.96 was used. The output was digitized and sampled at a rate of 1 kHz and on-line averaged over 8 s. To determine the visible flame height and flame blowout sequence, a high-speed digital video camera was used. The technique proposed by Yagi and Iino[18] was used to measure soot concentration. A He-Ne laser beam was passed through the flame, and its attenuation was measured using a pyro-electric laser power meter. The process was slightly modified by using a narrowband pass laser line filter to block the luminous flame background and Rayleigh scattering from the soot particles. The experimental details of various measurements can be found elsewhere.[19] A computer-controlled monochromator with input and output focal lengths of 220 and 257.36 mm, respectively, was used in this experiment for emission spectral measurement. The monochromator had a variable width rectangular slit. A portion of the flame image (4 cm high from the burner tip and 2.8 cm thick) was focused on the monochromator's slit, and the slit width was adjusted to capture the whole width of the flame. The light intensity at the desired wavelength was monitored by a high-sensitivity photomultiplier tube. The monochromator was scanned from 200- to 650-nm wavelengths with 1-nm step. The output from the photomultiplier was linearly proportional to the power at a particular wavelength. The output of the photomultiplier tube at a particular wavelength was sampled at 1 kHz rate and on-line averaged over 5 s. The nominal operating conditions and experimental uncertainties are listed in Tables 1 and 2.

Table 1 Nominal operating conditions

Parameter	Value
2:1 Aspect ratio elliptic coflow	
Major axis diameter	0.036 m
Minor axis diameter	0.018 m
Coflow Reynolds number (minor axis)	4010
Coflow Reynolds number (major axis)	8020
4:1 Aspect ratio elliptic coflow	
Major axis diameter	0.051 m
Minor axis diameter	0.013 m
Coflow Reynolds number (minor axis)	2837
Coflow Reynolds number (major axis)	11348
Circular coflow	
Diameter	0.026 m
Coflow Reynolds number	5674
Coflow velocity	3.45 m/s
Burner jet-exit diameter (ID)	0.004 m
Burner jet-exit velocity (ID)	3 m/s
Burner jet-exit Reynolds number	2700
Fuel	Propane, (95% C_3H_8, 3% CH_4,1% C_2H_6, 1% C_4H_{10}) Hydrogen (98%+)
Fuel density	1.813 kg/m^3
Lower heating value	46357 kJ/kg
Absolute viscosity	8×10^{-6} N · s/m^2
Ambient conditions	
Temperature	294 K
Pressure	100.6 kPa
Relative humidity	58%
Froude number	
Jet-exit Froude number	231
Global flame Froude number	0.077
Densimetric Froude number	671

Table 2 Estimated measurement uncertainties (based on student's t-test at 95% confidence interval)

Measurement	Symbol	% of mean value
Temperature	T	4
Concentration of NO	XNO	12.2
Concentration of O_2	XO_2	7.8
Concentration of CO_2	XCO_2	5.5
Concentration of CO	XCO	5
Soot concentration	w	12
Radiative heat fraction	F	1.5
Flame velocity	V	4
Flame height	L	16
Emission spectra	V	2

Results and Discussion

Flame Length

Figure 2 shows the variations in visible flame height as a function of coflow velocity. The flame height was normalized by the circular coflow diameter. At low coflow velocities (that is, low Reynolds number) the flames are laminar, with sharp edges and steady in shape. In general, from Fig. 2 it can be deduced that the flame height in the elliptic coflow decreases at a faster rate than in the circular coflow with the increase in coflow velocity.

Direct color photographs of the flames (color photographs are available in Luna[19]) indicate that the visible height of the flames in the circular coflow decreases slightly with an increase in coflow velocity. At a coflow velocity of 1.46 m/s, the flame edges and tip become wrinkled as a result of the onset of instabilities. With a further increase in coflow velocity, the flame height decreases. The decrease, however, is not very apparent in the case of the flames in circular coflow. The decrease in flame height is caused by the entrainment of air through coflow. With the increase in coflow velocity, the fuel has to travel a shorter distance in order to attain the required oxidizer, hence the mixing takes a shorter time. Consequently, a shorter diffusion flame is produced. Also, the 4:1 aspect ratio (AR) elliptic coflow flame entrains more air than the 2:1 AR elliptic and circular coflow flames. At a coflow velocity of 3.22 m/s, for example, the normalized flame height of the circular coflow flames, the 2:1 AR elliptic coflow flame and the 4:1 AR elliptic coflow flame are 20, 18.25, and 15, respectively. This clearly indicates the higher air entrainment in the elliptic coflow flames.

Flame Stability

Stability Curve

The stability diagram (blowout) of flames with elliptic and circular coflow is shown in Fig. 3. In general, at a low fuel jet-exit velocity flames in circular coflow withstand a higher coflow velocity than in elliptic coflow. However, as the aspect ratio of the elliptic coflow is increased to 4:1 the flame stability increases again. In fact, the stability behavior of the circular and 4:1 AR elliptic coflow is almost identical except at a very low jet-exit velocity. At a high fuel jet-exit velocity ($U_j > 12$ m/s) the stability behavior of flames with all three coflow configurations is the same. At a low fuel jet velocity (1.5 m/s) a stable lifted flame exists with the circular coflow, and the flame blowsout at a relatively high coflow velocity ($U_c = 3.6$ m/s). In contrast, at the same jet-exit velocity the flame with 2:1 AR coflow blows out at a lower coflow velocity. The near-field entrainment of the elliptic jets is much higher than that of the circular counterpart. For this reason, the lean blowout of the 2:1 AR elliptic coflow flames occurs earlier than in a circular coflow. However, as the aspect ratio increases from 2:1 to 4:1 the length of the major axis increases, which delays the leaning of fuel along that axis. As a result, despite the increase of mixing through minor axis, the fuel-air mixture remains within flammability limits in some portion of the major axis. For this reason, the flame with higher aspect ratio coflow exhibits a higher stability.

As the fuel jet velocity increases from 1.5 to 3.3 m/s, the base of the lifted flame becomes unstable, and the flame blows out at smaller coflow velocities. This trend is significant for all three coflow configurations. This marks the beginning of the turbulent blowout regime. With a further increase of fuel jet velocity, the coflow velocity required to cause flame blowout increases for both circular and elliptic configurations until the stability behavior for both the elliptic and circular coflow flames seems identical. This identical trend is probably because at a sufficiently high jet velocity blowout is mostly dominated by the fuel jet characteristics rather than the coflow.

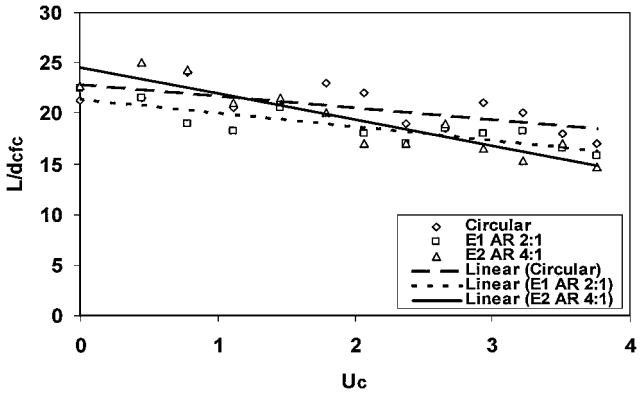

Fig. 2 Variation of flame length with increase in coflow velocity.

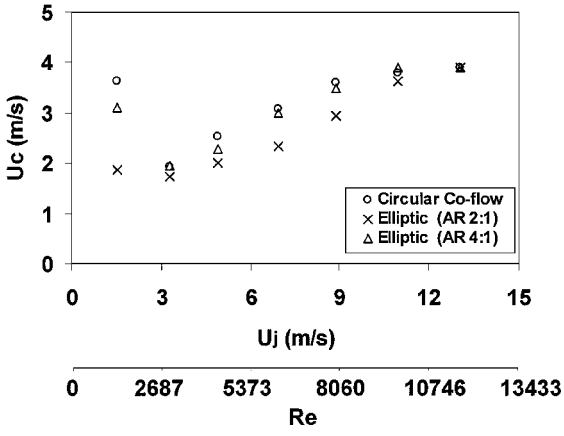

Fig. 3 Flame stability curves of flames with circular, 2:1 and 4:1 AR coflows.

Blowout Images

Figure 4a shows the photographic sequence preceding flame blowout with the increase in coflow velocity for the flames with the circular, 2:1 AR elliptic, and 4:1 AR elliptic coflow, respectively. The fuel flow velocity was kept constant at 1.5 m/s while the coflow velocity was increased from 0 m/s to the point at which the flame blows out. The 2-s interval blowout sequence images are presented for all of the configurations.

In all of the figures, it is seen that as the coflow velocity increases the flames become shorter because the fuel has to travel a shorter distance to mix with the surrounding air. Flame blowout occurs when the local flow velocity exceeds the flame speed or local extinction occurs. As the coflow velocity increases, the flame at first lifts off from the burner mouth, and a further increase in coflow velocity causes the flame blowout. While comparing the photographs, it can

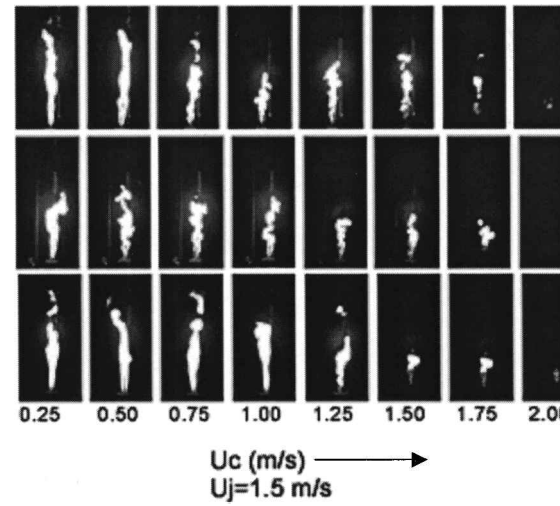

Fig. 4a Photographic sequence preceding blowout with the increase in coflow velocity. Fuel jet velocity (U_j) = 1.5 m/s; top row, circular; middle row, 2:1 elliptic; bottom row, 4:1 elliptic.

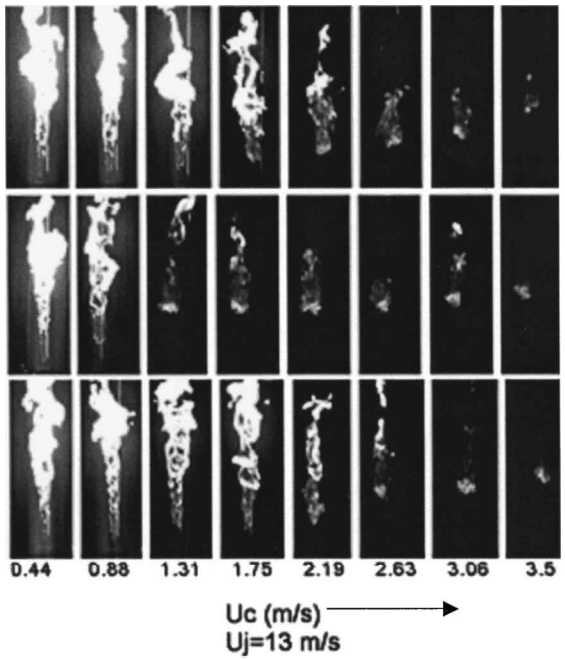

Fig. 4b Photographic sequence preceding blowout with the increase in coflow velocity. Fuel jet velocity (U_j) = 13 m/s; top row, circular; middle row, 2:1 elliptic; bottom row, 4:1 elliptic.

be seen that at a fixed fuel velocity of 1.5 m/s the flame with the circular coflow is more stable than the 4:1 AR elliptic coflow flame and the 2:1 AR elliptic coflow flame. The 2:1 AR coflow flame blows out at approximately 1.86-m/s coflow velocity. At this coflow velocity the circular and the 4:1 AR elliptic coflow flames still persist. It is also observed that the 4:1 AR elliptic coflow flame blows out at a coflow velocity of 3.09 m/s and the circular coflow flame blows out at 3.63 m/s. The near-field entrainment of the elliptic jets is higher than that of the circular jets. For this reason, the elliptic coflow flames become unstable, and hence the blowout occurs earlier than in a circular coflow. This is in agreement with Fig. 3, which shows that at a fixed fuel flow velocity of 1.5 m/s the coflow velocity required to cause flame blowout with the circular and 4:1 AR coflows is higher than in the 2:1 AR coflow.

Figure 4b shows the photographic sequence at 13.07-m/s fuel jet velocity with the increase in coflow velocity for the flames with the circular, 2:1 AR elliptic, and 4:1 AR elliptic coflow respectively. All of the images show that at this high fuel velocity flames are initially lifted and the flame stability behavior is similar. All of the flames blow out at approximately the same coflow velocity of 3.6 m/s in conformity with the results shown in Fig. 3.

Emission Indices

The pollutant emission indices[2] defined as the amounts of pollutants produced per kilogram of fuel burned are shown in Fig. 5. {The emission index (EI) of a species, defined as the mass of the species emitted per unit mass of the fuel burned, was calculated using the equation $EI_i = [\chi_i/(\chi_{co2} + \chi_{co})][nMw_i/MW_f]$, where χ is mole fraction, n is the number of carbon atoms in fuel, and MW_i and MW_f are the molecular weight of the species and the fuel, respectively.} The flames with the elliptic coflow produce a higher amount of nitric oxide than in the circular coflow flame. Also, the 4:1 AR flame produces higher NO than the 2:1 AR coflow. The 4:1 AR elliptic geometry causes high turbulence compared to the 2:1 AR elliptic and circular geometries, which adds to the existing turbulence level of the flames in the near-burner regions. More fuel is pushed into the downstream regions of flames, increasing the postflame gas temperature. This prompts more nitric-oxide formation through the recombination reactions of molecular nitrogen and oxygen of the incoming air.

The carbon-monoxide emission index is lower in the elliptic coflow flames than in the circular coflow flames. The comparison

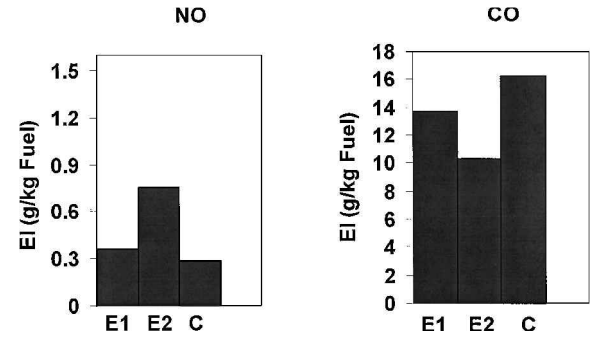

Fig. 5 Emission indices of flames with circular, 2:1 and 4:1 AR coflows.

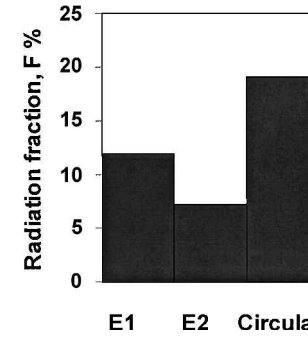

Fig. 6 Flame radiation fraction from the flames with circular, 2:1 and 4:1 AR coflows.

of emission indices of the 4:1 and 2:1 AR elliptic coflow flames reveals that the 4:1 AR coflow flame produces less CO than the 2:1 AR coflow flame. The results clearly indicate the oxygen-enriched combustion in the elliptic coflow configuration. In circular coflow the lower availability of air limits the carbon monoxide oxidation reaction ($CO + O_2 \rightarrow CO_2 + O$), which in turn restricts the production of OH radical ($O + H_2O \rightarrow OH + OH$) and thereby reduces CO destruction through the CO and OH recombination reaction ($CO + OH \rightarrow CO_2 + H$). Hence, the CO emission is higher in the circular coflow flame. On the other hand, the low concentration of oxygen limits the NO formation through the extended Zeldovich route ($O + N_2 \rightarrow NO + N$; $N + O_2 \rightarrow NO + O$; $N + OH \rightarrow NO + H$). For this reason, NO emission is lower in circular coflow. Because CO and NO both compete for oxygen, one pollutant increases at the expense of the other.

Radiative Fraction of Heat Release

Figure 6 shows the radiation fraction of heat release for the circular, 2:1 and 4:1 AR coflow flames. The radiation emission of all flames lies within a range of 5–20% of their total energy input. It is clear that the circular coflow flame radiates the most, followed by the 2:1 AR coflow flame and the 4:1 AR elliptic coflow flame. It is seen that the circular coflow flame radiation fraction is 7.9 and 11.8% more than that of the 2:1 and 4:1 AR elliptic coflow flames, respectively. The radiation fraction of gaseous jet flames depends on many factors: temperature, fuel type, sooting tendency, and the stoichiometry of the oxidizer-fuel mixture. From Fig. 7 it is clear that the circular coflow flame is more sooty than the 2:1 and 4:1 AR elliptic coflow flames. For that reason, the circular coflow flame radiation fraction is larger. Comparing the 2:1 and 4:1 AR elliptic coflow flames, it is seen that in the 2:1 AR coflow flame radiation fraction is 4% more than the 4:1 AR coflow flame. Because there is more air entrainment in the 4:1 AR coflow flame, more oxygen is available in the near-nozzle region to reduce the soot formation, hence reducing the flame sooting characteristics.

Soot Concentration

It is generally agreed that in diffusion flames soot is formed in the temperature range of 1300–1600 K (Ref. 20). In diffusion flames

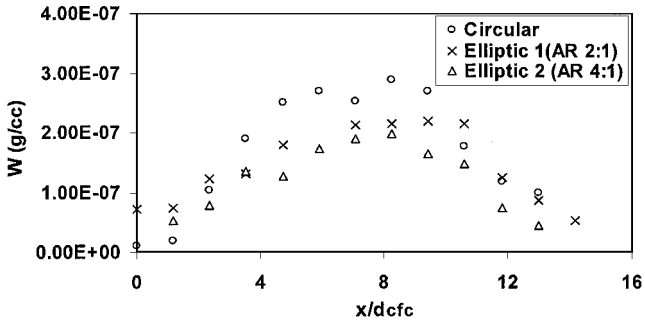

Fig. 7 Axial profiles of soot concentration in the flames with circular, 2:1 and 4:1 AR coflows.

soot forms in the fuel-rich near-burner region and burns out in the far-burner region. Figure 7 presents the axial distribution of soot concentration in flames with elliptic and circular coflow. In general, the flames of all of the configurations show, 1) soot inception in the near-burner region, 2) growth in the midflame, and 3) burning in the far-burner region. While comparing the elliptic and circular coflow flames, it is seen that the flames in elliptic coflow produce less soot than in circular coflow. Also, the 4:1 AR elliptic coflow flame produces less soot than the 2:1 AR coflow flame. This is an effect of the higher air entrainment in the 4:1 AR elliptic coflow flame, which limits the formation of soot precursors such as polycyclic aromatic hydrocarbons and thereby reduces soot formation in the near-burner region. The higher air entrainment also results in more soot oxidation in the elliptic coflow flames. For this reason, in the far-burner region ($x/d_{\mathrm{cfc}} > 10$) soot concentration is lower in the elliptic coflow flames than in the circular coflow flame.

Radiation Spectral Measurements

The near-burner emission spectra of flames at different coflow configurations are shown in Fig. 8. The flame radiation emission was collected by focusing a portion of the flame on a rectangular slit of a monochrmoator. The collection area was 4 cm in axial (starting from burner tip) and 2.8 cm in the radial direction. The details of the measurement techniques are discussed in Luna.[19] Because the primary objective of this measurement was to identify the qualitative trend of OH and CH radical formation to verify the aforementioned arguments, the spectral scans were limited to 200-nm through 650-nm wavelength where the strong bands of OH and CH existed. The signals were normalized using the flame thickness to account for the variations of the reaction zone thickness.

Different bands of OH [(2, 0), (1, 0), (3, 2), and (0, 0)] are detected in the emission spectra. It is observed that the OH radical formation is higher in the elliptic coflow flames than in the circular coflow flame. In fact, OH (2, 0) and OH (1, 0) bands are not detected in the circular flow flame. Because the formation of OH radicals can be directly related to the rate of fuel pyrolysis reactions, it can be inferred that the near-burner entrainment increases, which enhances the fuel oxidation rate in the elliptic coflow. The overall OH radical production rate in the 4:1 AR elliptic coflow is higher than that in the 2:1 AR elliptic coflow. This supports the argument that the 4:1 AR elliptic coflow flame has a higher entrainment than the 2:1 AR elliptic coflow flame. Similarly, the production of CH radical is also higher in the elliptic coflow flames. CH radical is a key indicator of fuel oxidation reactions. Hence, an increase of CH signal in emission spectra points to the increase of fuel oxidation in the near-burner location of the elliptic coflow flames. Two CH bands, (0, 0) and (1, 0) are detected in the spectral scan. Although the change in CH (0, 0) band with coflow configuration is insignificant, the signal from CH (1, 0) band increases as coflow changes from circular to 2:1 AR elliptic and then to 4:1 AR elliptic. Other species detected in the spectral scan are C_2 and H_2O. Two different bands of C_2, (1, 0) and (0, 0), are identified. The C_2 radicals form as a result of the initial breakdown of the fuel, which later leads to the formation of other active radicals such as CH, OH, and H through various intermediate reactions ($C_2H + O_2 \rightarrow CH + CO_2$; $C_2H + C_2H_2 \rightarrow C_4H_2 + H$; $H + O_2 \rightarrow OH + O$). Hence, an increase of C_2 formation indicates a higher level of fuel breakdown, which is evident in flames with elliptic coflow. The elliptic coflow flames have higher C_2 signals than that of the circular coflow flame. A strong H_2O line is detected in the flame spectra. This is primarily because of the addition of hydrogen to anchor the flame. Similar to CH and OH, the elliptic coflow flames have a higher H_2O signal than that of circular coflow flame.

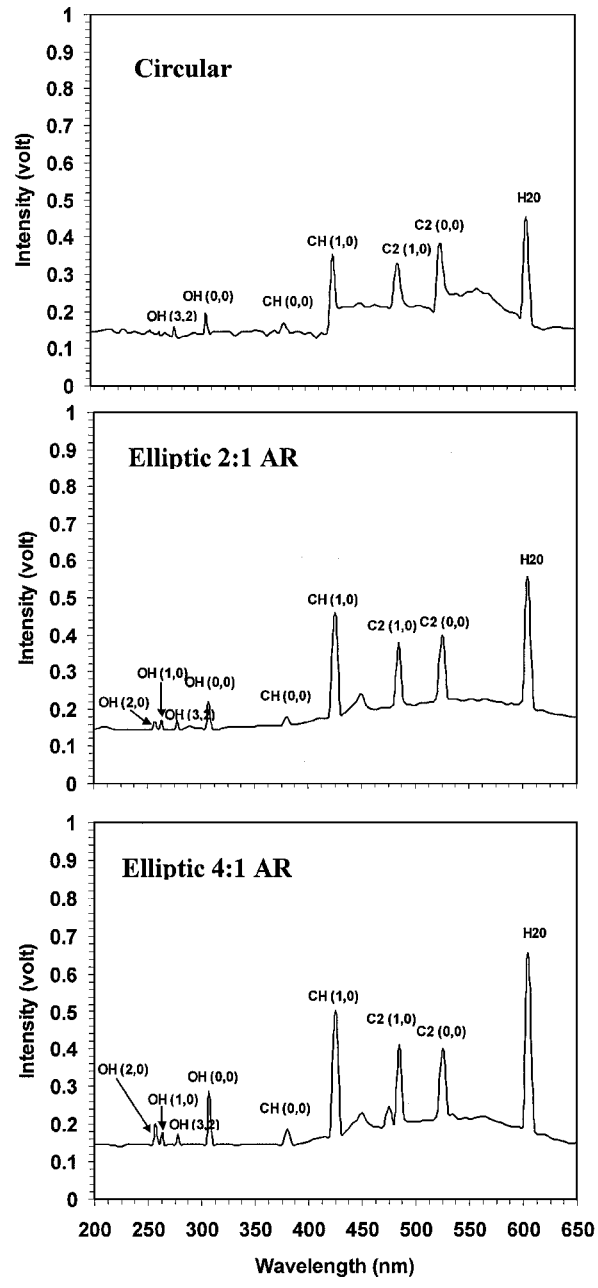

Fig. 8 Radiation spectral measurements from the flames with circular, 2:1 and 4:1 AR coflows.

Flame Structure

The visible flame length was divided into three distinct regions: the near-burner region, the midflame region, and the far-burner region. Radial temperature and species concentration profiles were obtained in each of these three regions. In this paper the profiles in only circular and 2:1 AR elliptic coflow flames are presented. The corresponding data from 4:1 AR coflow elliptic flames are given in Luna.[19]

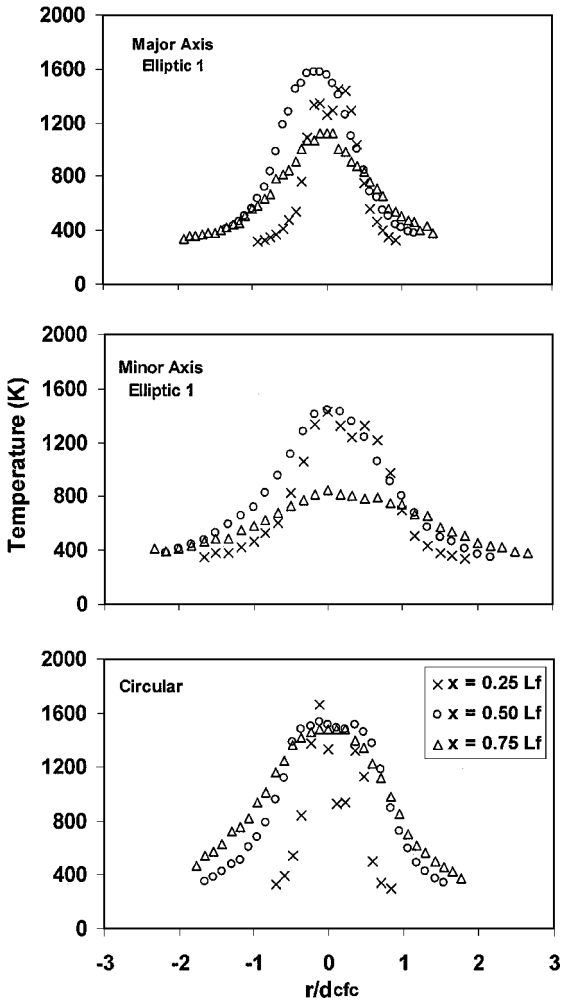

Fig. 9 Radial temperature profiles in flames with the 2:1 AR elliptic and circular coflows. U_c = 3.45 m/s; U_j = 3 m/s.

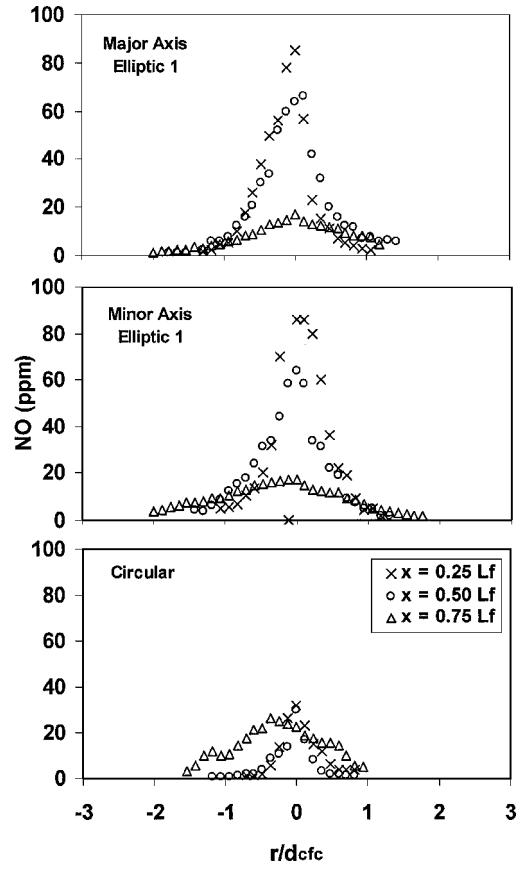

Fig. 10 Radial NO concentration profiles in flames with the 2:1 AR elliptic and circular coflows. U_c = 3.45 m/s; U_j = 3 m/s.

Flame Temperature

The radial temperature profiles for the 2:1 AR coflow flames and the circular coflow flames are shown in Fig. 9. It is seen that in the near-burner and midflame regions the temperature profiles do not look symmetrical. This could be because of the flow disturbances caused by the sidewise insertion of thermocouple. In the near-burner region (at 25% of the flame height) both elliptic and circular coflow flames show temperature profiles with twin peaks located approximately 0.5 diam (equivalent) away from the flame axis. In the midflame region the peaks are less apparent, and the temperature gradient is not as steep as in the near-burner region. The twin peaks vanish in the far-burner region, and a single peak appears indicating the reaction zone has penetrated into the entire radial plane.

While comparing the circular and the 4:1 and 2:1 AR elliptic coflow flames, it is found that the twin-peak structure is more prominent in the former. This indicates that in the circular coflow flame reactions are mostly confined to a thin stoichiometric contour where incoming oxidizer meets outwardly moving fuel stream. On the other hand, in the elliptic coflow flame this reaction zone is much thicker. The elliptic coflow flames exhibit a lower peak temperature in the near-burner region, especially along the minor axis, and a higher valley temperature compared to the circular coflow flames. This is an indication of better mixing caused by the elliptic coflow geometry. The nonaxisymmetric geometry entrains more ambient air, which lowers the peak temperature at flame edges and moves more air to the jet core. Therefore, at the jet core the reaction rate increases, which results in the increase of valley temperature. The jet growth and dilution caused by entrainment are stronger along the minor axis than on the major axis resulting in a lower peak temperature on the minor axis.

In the midflame region the peak temperature of the circular and elliptic coflow flames is comparable. Farther downstream, the soot growth and oxidation reaction proceed along the flame centerline. As discussed earlier, because the elliptic coflow has a higher radial spreading rate the far-burner temperature profile in the flame with elliptic coflow is comparatively flatter than in circular coflow. Also, the temperature is lower in the elliptic coflow flame, especially along the minor axis.

Nitric-Oxide Concentration Profiles

Radial profiles of NO concentration at different axial locations are shown in Fig. 10. The NO profiles in the near-burner region generally follow the temperature profiles. In this region the formation of NO on both the major and minor axes of the 2:1 AR elliptic coflow flame are higher than that in the circular coflow flame. The valley temperatures of the elliptic coflow flames are higher, which results in a larger production of NO through the Zeldovich mechanism in the elliptic coflow flames. Although the peak flame temperature is comparable in elliptic and circular coflow flames, it is the higher oxygen availability, which triggers higher NO formation in the elliptic coflow flames. While comparing the peak NO concentration in the elliptic and circular coflow flames, it is observed that the 2:1 AR elliptic coflow flame produces about 80% more NO than the circular coflow flame. As discussed in conjunction with emission indices, the favorable flame temperature and higher oxygen concentration in flame core lead to significantly higher NO formation through the extended thermal Zelodvich route in the elliptic coflow flame. The NO concentration profiles in the midflame region also reveal that the circular coflow flame produces less NO than its elliptic counterpart. The 2:1 AR elliptic coflow flame produces 78% more NO than the circular coflow flame. Higher temperature in the elliptic coflow flame contributes to this difference. Also, because of higher air entrainment in the elliptic coflow flames the stoichiometry shifts

slightly toward the fuel-lean side, resulting in more NO production. The elliptic coflow flame produces about the same amount of NO in this region. The higher soot concentration in this region appears to mask the effect of increased air entrainment. In the far-burner region the NO concentrations in the elliptic coflow flames have dropped by significant amounts. For example, in the 2:1 AR elliptic coflow flame the NO concentration level drops from 66–85 ppm range to 17–20 ppm range. This behavior is qualitatively similar to the temperature profile. However, in the circular coflow flame the reduction in NO formation is not very significant. The NO concentrations in the circular coflow flame seem to be low in all of the regions. The drop in the NO concentration in all of the flames can be attributed to the low temperature. Because the flame temperatures are low in this region, the NO production through the Zeldovich mechanism is small. The prompt and fuel NO formations occur very rapidly and are usually completed in the near-burner and midflame regions. The NO produced in the midflame and near-burner region might have passed into the far-burner region where its concentration would reduce because of dilution and conversion into NO_2 and N_2. (Refs. 21 and 22).

Carbon-Monoxide Concentration Profiles

The radial concentration profiles of CO at different axial locations are shown in Fig. 11. The elliptic coflow flame produces less CO than the circular coflow flame in the near-burner, midflame, and far-burner regions. The circular coflow flames produce about 6% more CO than the 2:1 AR elliptic coflow in the near-burner region. This can be attributed to the higher air entrainment in the elliptic coflow. Because a significant amount of oxygen is available in this region for the elliptic coflow flame as a result of a greater entrainment, most of the carbon monoxide that is formed is converted to carbon dioxide. In the midflame region the peak CO concentration levels drop by 26% in the 2:1 AR coflow flames and 25% in the circular coflow flames. The circular coflow flames yield higher CO concentrations than the elliptic coflow flames in this region also for the same reasons as mentioned earlier. In the far-burner region because of the dominant soot oxidation process carbon-oxygen reaction begins. Because circular coflow has a lower entrainment and thus lower oxygen concentration, the reaction forms more CO than CO_2. For this reason, the CO concentration levels in the far-nozzle region of the circular coflow flames are relatively higher than the corresponding values in the elliptic coflow flame.

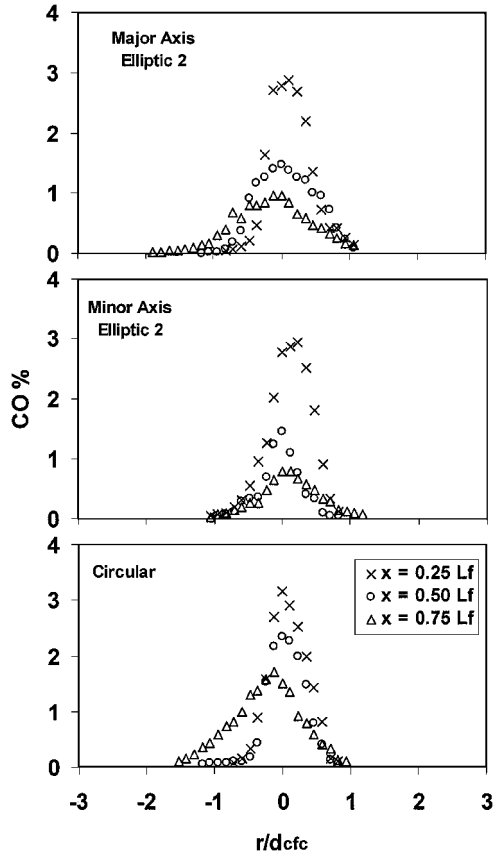

Fig. 11 Radial CO concentration profiles in flames with the 2:1 AR elliptic and circular coflows. U_c = 3.45 m/s; U_j = 3 m/s.

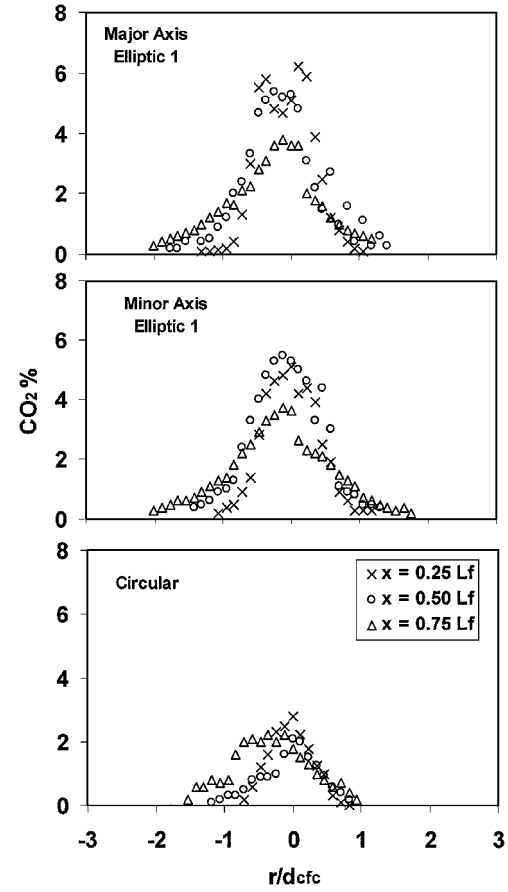

Fig. 12 Radial CO_2 concentration profiles in flames with the 2:1 AR elliptic and circular coflows. U_c = 3.45 m/s; U_j = 3 m/s.

Carbon-Dioxide Concentration Profiles

The radial profiles of CO_2 concentrations are shown in Fig. 12. The CO_2 profiles generally follow the profiles of flame temperature. In general, the circular coflow flames produce the least amount of carbon dioxide. Circular coflow flames are highly sooty flames, and thus in the near-burner regions carbon atoms are absorbed in the PAH formation resulting in a lower CO_2 formation. The double hump in the near nozzle regions of the elliptic and circular coflow flames are clearly seen in the figures. The double humps become flatter in the midflame and far-burner regions. Because elliptic coflow entrains more air, soot oxidation is more prominent. As a result, combustion is enhanced as a result of higher oxygen availability and soot oxidation reaction, and thus a higher yield of CO_2 concentration is obtained.

Oxygen Concentration Profiles

Figure 13 shows the radial concentration profiles of O_2. The radial profiles of oxygen appear like a U shape with a broad base as expected. The oxygen concentration in the 2:1 AR elliptic coflow flame drops from 21.7 to 3.9% within a radial distance of $r/d_{\text{cfc}} = \pm 3.0$. This significant amount of oxygen concentration drop is caused by the high chemical activity in this region. Thus most of oxygen entrained is consumed. In the circular coflow flame oxygen concentration varies from 20.6 to 10.6% within a radial distance

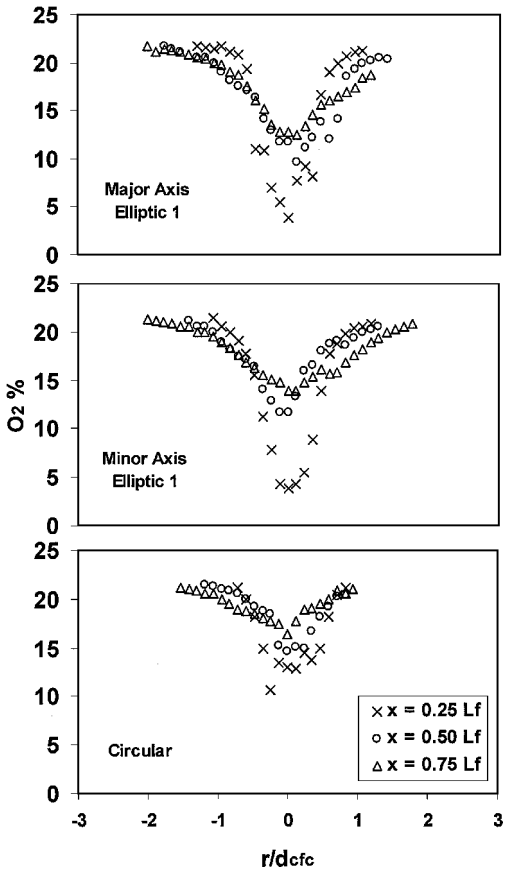

Fig. 13 Radial O_2 concentration profiles in flames with the 2:1 AR elliptic and circular coflows. U_c = 3.45 m/s; U_j = 3 m/s.

of $r/d_{\text{cfc}} = \pm 0.8$. The oxygen concentration profiles in the elliptic coflow flame are wider than those in the corresponding circular coflow flame because of the higher spreading rate of the former. The oxygen concentration profile in the valley of the circular coflow flame is 63% higher than the 2:1 AR coflow flame. This shows that in the elliptic coflow flame whatever air reaches the flame core is being used up at a faster rate than in the circular coflow flame, thus indicating a better fuel-air mixing. In the midflame region also the oxygen concentration profiles in the elliptic coflow flames are also wider than those in the circular coflow flame, showing a higher spread in the elliptic coflow flame. In the valley of the 2:1 AR coflow flame, the O_2 concentration is 5% lower than in the circular coflow flame. This shows that in the midflame region the elliptic coflow flame consumes a larger amount of oxygen and that oxygen is fully utilized in this region to convert CO into CO_2. In the far-burner region the flame core contains a significantly large amount of air. The O_2 profiles in this region have broadened. The circular coflow flame contains 3.6% more O_2 than the 2:1 AR elliptic coflow flames. These observations suggest that the elliptic coflow flame has a superior combustion efficiency.

Conclusions

This paper presents an experimental study to understand the effects of coflow geometry on gas jet flame characteristics. The effects of elliptic coflow on flame characteristics are studied and compared with the effects of a circular coflow, which is used as the baseline condition. The fuel jet-exit velocity and coflow velocity are 3 and 3.45 m/s, respectively. Global flame characteristics (stability, emission indices, and flame radiation) and flame structure (flame velocity, soot concentration, flame temperature, and species concentration profiles) are measured to delineate the effects of coflow geometry on flame characteristics.

The overall trends of the measured flame parameters showed that the flames with the elliptic coflow geometry, in general, have superior combustion characteristics than the flames in a circular coflow. The elliptic coflow flames are shorter, radiate less, yield less soot, yield higher valley temperature and lower peak temperatures, produce more NO and less CO compared to the flames in a circular coflow. These changes are attributed to the azimuthal instabilities that occur in elliptic coflow, which help in entraining more surrounding air, and thus enhance combustion characteristics. As a result of higher entrainment of air, more oxygen is available to aid combustion, and hence soot oxidation is enhanced. Thus the elliptic coflow flame radiates less than the circular coflow flame and also leads to a higher CO_2. The flames with elliptic coflow can withstand a lower coflow velocity before blowout than circular coflow flames. The present investigation demonstrates that a burner system incorporating the elliptic coflow geometry might be employed in gas-turbine combustor applications. Because these applications require low flame radiation to reduce the heat loading on combustion chamber liners materials, an elliptic coflow configuration, which yields a low flame radiation, is a potential solution.

Acknowledgments

The financial support from the Graduate College and Graduate Student Senate of the University of Oklahoma as a dissertation research grant to Ahsan R. Choudhuri and a research and creativity grant to Sayela P. Luna are acknowledged. Authors also acknowledge Ryan Wicker, University of Texas El Paso, for his valuable suggestions while preparing the manuscript. Appreciations are extended to Benjamin Baird, Sien F. Goh, and Jordi Carrera for their help in experiments.

References

[1]Kolluri, P., Kamal, A., and Gollahalli, S. R., "Application of Elliptical Primary-Air Inlet Geometries in the Inshot Burners of Residential Gas Furnaces," *Journal of Energy Resources Technology*, Vol. 118, No. 2, 1996, pp. 58–64.

[2]Gollahalli, S. R., and Subba, S., "Partially Premixed Laminar Gas Flames from Triangular Burners," AIAA Paper 96-0285, Jan. 1996, also *Journal of Propulsion and Power*, Vol. 13, No. 2, 1997, pp. 226–232.

[3]Gollahalli, S. R., "Jet Flames from Noncircular Burners," *Journal of Indian Academy of Sciences*, Vol. 22, Pt. 3, 1997, pp. 369–382.

[4]Gollahalli, S. R., "Effect of Flame Lift-off on the Differences Between the Diffusion Flames from Circular and Elliptic Burners," *Journal of Energy Resources Technology*, Vol. 120, No. 2, 1998, pp. 161–166.

[5]Ho, C.-M., and Gutmark, E., "Vortex Induction and Mass Entrainment in a Small-Aspect-Ratio Elliptical Jet," *Journal of Fluids Mechanics*, Vol. 179, June 1987, pp. 383–405.

[6]Schadow, K. C., Gutmark, E., Koshigoe, S., and Wilson, K. J., "Combustion-Related Shear-Flow Dynamics in Elliptic Supersonic Jets," *AIAA Journal*, Vol. 27, No. 10, 1989, pp. 1347–1353.

[7]Wicker, R. B., and Eaton, J. K., "Effect of Injected Longitudinal Vorticity on Particle Dispersion in a Swirling, Coaxial Jet," *Journal of Fluids Engineering*, Vol. 121, No. 4, 1999, pp. 766–772.

[8]Wicker, R. B., and Eaton, J. K., "Structure and Control of a Particle-Laden Coaxial Jet with or without Annular Swirl," Thermosciences Div., Dept. of Mechanical Engineering, Stanford Univ., Rept. MD-68, CA, Dec. 1994.

[9]Longmire, E. K., and Eaton, J. K., "Structure of a Particle-Laden Round Jet," *Journal of Fluid Mechanics*, Vol. 236, March 1992, pp. 217–257.

[10]Hussain, F., and Hussain, H. S., "Elliptical Jets. Part 1. Characteristics of Unexcited and Excited Jets," *Journal of Fluid Mechanics*, Vol. 208, Nov. 1989, pp. 257–320.

[11]Sforza, P. M., Steiger, M. H., and Trentacoste, N., "Studies on Three-Dimensional Viscous Jets," *AIAA Journal*, Vol. 4, No. 5, 1966, pp. 800–806.

[12]Quinn, W. R., "The Turbulent Free Jet Issuing from a Sharp-Edged Elliptical Slot," AIAA Paper 89-0664, Jan. 1989.

[13]Gollahalli, S. R., Khanna, T., and Prabhu, N., "Diffusion Flames of Gas Jets Issued from Circular and Elliptic Nozzles," *Combustion Science and Technology*, Vol. 86, Nos. 1–6, 1992, pp. 267–288.

[14]Krothapalli, A., Baganoff, D., and Karamcheti, K., "On the Mixing of a Rectangular Jet," *Journal of Fluid Mechanics*, Vol. 107, June 1981, pp. 201–220.

[15]Prabhu, N., and Gollahalli, S. R., "Comparison of Gas Jet Flames over Circular and Elliptic Nozzles," Combustion Inst., Paper 42, March 1989.

[16]Kamal, A., "Turbulent Diffusion Gas Jet Flames from Circular and Elliptic Nozzles," Ph.D. Dissertation, School of Aerospace and Mechanical Engineering, Univ. of Oklahoma, Norman, OK, 1995.

[17]Fristrom, R. M., and Westenberg, A. A., *Flame Structure*, McGraw–Hill, New York, 1965, pp. 17–26.

[18]Yagi, S., and Iino, H., "Radiation from Soot Particles in Luminous Flames," *Proceedings of the Eighth International Symposium on Combustion*, Combustion Inst., Pittsburgh, PA, 1960, pp. 288–293.

[19]Luna, S. P., "Effects of Nonaxisymmetric Coflow on Diffusion Flames," M.S. Thesis, School of Aerospace and Mechanical Engineering, Univ. of Oklahoma, Norman, OK, 2001.

[20]Turns, S. R., *An Introduction to Combustion-Concepts and Application*, McGraw–Hill, New York, 1997, pp. 291–295.

[21]Borghi, R., "New Results of Studies of Combustion Flows Obtained at ONERA," *Combustion Measurements—Modern Techniques and Instrumentation*, edited by R. Goulard, Hemisphere, New York, 1974, pp. 318–324.

[22]Cernasky, N. P., and Sawyer, R. F., "NO and NO2 Formation in a Turbulent Hydrocarbon/air Diffusion Flame," *Proceedings of the Fifteenth International Symposium on Combustion*, Combustion Inst., Pittsburgh, PA, 1976, pp. 1039–1050.